Efficient and Accurate Method for Calculating and Representing Power Density in the Near Zone of Microwave Antennas

RICHARD L. LEWIS, SENIOR MEMBER, IEEE, AND ALLEN C. NEWELL, SENIOR MEMBER, IEEE

Abstract—**An efficient and reliable method has been developed for computing and exhibiting Fresnel-region fields radiated by microwave antennas using plane-wave scattering matrix analysis. That is, we calculate near fields by numerically integrating the complex far-field antenna pattern. The predicted near fields are exhibited as relative power-density contours lying in a longitudinal plane bisecting the antenna's aperture. With spatial coordinate scaling, each set of contours becomes a function of the relative aperture distribution and the electrical size of the antenna. If the electrical diameter is much larger than any normalized transverse coordinate of interest, the contour set becomes invariant with respect to antenna size. Thus coordinate normalization can produce contours applicable to any antenna with the same relative aperture distribution, regardless of antenna size. The crux of the analysis consists of handling a numerical instability which arises from integrating discrete data. A criterion is developed for excluding highly oscillatory regions of the integrand. In turn, this leads to restricting the output domain where the near field computations are valid. With the numerical instability problem resolved, the fast Fourier transform is used for efficient numerical integration. The predicted near fields have been compared against both measured and theoretical data, confirming that our near-field computation algorithm is capable of extremely high accuracy.**

I. Introduction

IN A NUMBER of situations related to safety and interference, it is desirable to have a reliable and concise method of estimating the power density levels radiated by microwave antennas. We present a new technique for predicting near-field intensities using plane-wave scattering matrix theory [1] to produce accurate calculations along with a highly efficient method of graphically representing the results. Using this technique, comparisons of predicted and measured near fields were carried out for selected antennas and found to be in excellent agreement.

The algorithm for calculating near-zone and Fresnel-region fields radiated by a microwave antenna proceeds by numerically integrating the plane-wave spectrum integral representation for the field. Efficient numerical computation is assured by use of the fast Fourier transform (FFT) and by limiting the computation space to the antenna's two principal planes. An earlier algorithm was developed by Yaghjian [2] for carrying out such a numerical integration. However, computational stability can play a critical role in numerical integration. In particular, with discrete data the integral becomes unstable at the extremities of the integration range if the longitudinal or electrical-boresight distance is large. This problem is alleviated by limiting the integration domain and by truncating the lateral-coordinate range.

We determine an optimum integration-domain size as a function of the longitudinal distance and the spatial frequency data-point spacing interval. The latter is inversely proportional to the maximum lateral-coordinate range. Now the FFT computes near-field values throughout this range; however, the useful output range is designated the effective lateral-coordinate range and is empirically set at half this maximum-range size to avoid numerically unstable regions. Moreover, for consistent results, we find that limiting the integration domain requires that we set an upper bound on the longitudinal distance. Thus the effective lateral-coordinate range and the upper bound on the longitudinal distance together define a truncated cylindrical region that bounds the near-field computation range.

The far-field pattern is a function [3], [4] of the normalized variable $u = KD$, where D is the antenna diameter and $K = k \sin \theta$, $k = 2\pi/\lambda$ is the propagation constant, λ is the wavelength, and θ is the angular position of the observation point with respect to antenna boresight. Consequently, upon normalizing boresight distance z with respect to D^2/λ and the transverse or lateral coordinates x and y with respect to D, it is readily shown that the near field is a function of just these normalized coordinates, the D/λ ratio, and the aperture distribution function. Moreover, if small structure effects contribute negligibly to the aperture distribution and the largest transverse coordinate of interest is small compared to D^2/λ, say for instance if $D \geq 30\lambda$ and the greatest effective lateral coordinate is $4D$, then the computed near fields become nearly independent of the D/λ ratio. Under these conditions our graphical results would apply to any size antenna with the same relative aperture distribution function. The most efficient method for exhibiting such results is a relative power-density contours in a plane formed by one lateral coordinate and the longitudinal coordinate. The power-density normalization is with respect to peak field intensity and may be converted to absolute power density by scaling.

In the general case our coordinate normalization scheme produces consistent contour plots for exhibiting and comparing results from different antennas. Usually, power-density contours for individual antennas would be normalized with respect to input power.

Manuscript received September 9, 1987; revised February 10, 1988.

The authors are with the Electromagnetic Fields Division, National Bureau of Standards, Boulder, CO 80303.

IEEE Log Number 8821103.

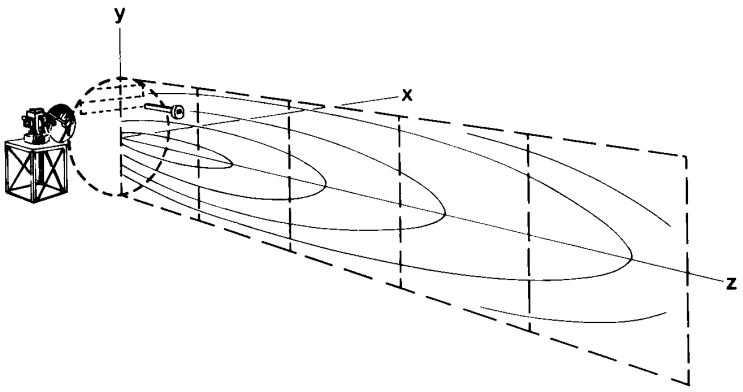

Fig. 1. Antenna measurement setup showing near-zone y–z plane cut on which field intensity contours are plotted.

We have generated near-zone predictions at distances corresponding to measured results and overlaid the plotted curves. The predictions have closely followed the measured results even when the field structure has varied rapidly. Moreover, our predictions agree closely with computations from an analytical expression for the on-axis field of a uniformly excited circular aperture. Having built confidence in our procedure, we go on to produce selected nomographs for obtaining absolute power densities in the near field of circular apertures with tapered aperture illuminations.

II. The Near-Field Computation Algorithm

Considerable attention has been given to the problem of calculating an antenna's far-field pattern from measured near-field data [5]–[14]. Of these techniques, planar near-field scanning (plane-wave spectrum deconvolution) has seen the most development [15]–[19]. Here, we consider the inverse problem, determining near-zone and Fresnel-region fields from numerical values of the complex vector far-field pattern. That is, we are interested in numerically evaluating the plane-wave spectrum integral representing the radiated electric field. The plane-wave spectrum input to the calculations can be obtained either from measured near-field data or theoretical analysis based upon antenna design specifications.

In Yaghjian's analysis of this problem [2], the integration domain was restricted to achieve computational efficiency; this also constrained the oscillatory nature of the integrand and so eliminated a catastrophic numerical instability which otherwise occurs at moderate z-axis distances. Extending this earlier work to discrete data with z-axis distances greater than $0.5D^2/\lambda$, we found numerical instabilities appearing at the extremities of the integration range. Attempts to reduce these instabilities by uniformly decreasing the already restricted integration domain drove the calculated field to zero at the extremities, an effect that had also been found by Yaghjian [2]. Uniformly enlarging the domain resulted in catastrophic disruption of the numerical integration. To compensate for these computational difficulties, a new limiting criterion was developed.

Yaghjian used a geometrical "sheaf of angles" criterion to limit the integration domain. In this work, we develop an improved formula for limiting the integration domain, using a sampling-theorem [20] criterion, producing a numerically stable result over a greater transverse output range. Also, we establish upper bounds on the z axis distance from the antenna and on the plane-wave spectrum's data-point spacing interval Δ to ensure reliable computations.

Evaluating the plane-wave spectrum integral, we compute near-zone and Fresnel-region fields at a sequence of fixed z-axis distances as a function of the lateral coordinates x and y. We reduce computational effort by alternately setting one lateral coordinate and then the other equal to zero. Thus, by computing along just the x and y axes, we obtain sufficient output to generate near-field intensity contours in the x–z and y–z planes.

To introduce notation, we digress to describe obtaining plane-wave spectrum data from planar near-field measurements. The measurement setup is depicted in Fig. 1, showing the antenna under test, the near-field measurement plane with the probe in front of the test antenna, and a hypothetical y–z plane cut through the cylindrical near-zone region of interest. The computed output is represented in the figure by field-strength contours in the y–z plane. At equally spaced intervals, vertical dashed lines represent fixed z-axis distances where the field is computed. Of course, for smooth contours more z-axis distances would be required than the figure indicates.

Measured data are taken at a series of equally spaced points over a planar surface in front of the test antenna. It is assumed that multiple reflections between the transmitting antenna and the probe are negligible, that both antennas are polarization matched in the same (y) direction, that input reflections at the antennas' waveguide feeds are negligible, and that the transmitting antenna is so far away that the probe's receiving pattern is essentially independent of spatial frequency variations, i.e., the incident radiation at the probe has a relatively narrow angle of arrival. Let $B_0(\mathbf{P})$ be the signal received by the probe at position $\mathbf{P}$ on the planar scan surface normalized to unity at position $\mathbf{P}'$ (here, $\mathbf{P} = x\mathbf{a}_x + y\mathbf{a}_y$, where $\mathbf{a}_x$, $\mathbf{a}_y$, $\mathbf{a}_z$ are unit Cartesian vectors), and let A_0 be the insertion loss between the transmitting antenna and the probe when it is located at position $\mathbf{P}'$. Then the dominant plane-wave spectrum's y component can be expressed [1], [15] as

$$b(\mathbf{K}) = \frac{1}{\lambda}\sqrt{\frac{2P_0}{\pi A_0 Y_0 G_r(0)}}\, e^{-i\gamma d} \iint_{-\infty}^{\infty} B_0(\mathbf{P}) e^{-i\mathbf{K}\cdot\mathbf{P}}\, d\mathbf{P} \quad (1)$$

where P_0 is the input power to the antenna, Y_0 is the characteristic admittance of free space, $G_r(0)$ is the gain of the probe, d is the z-axis distance from the planar scan surface to the transmitting antenna, $d\mathbf{P} = dxdy$, $\mathbf{K} = k_x\mathbf{a}_x + k_y\mathbf{a}_y$, and $\gamma = \sqrt{k^2 - K^2}$ where $k = 2\pi/\lambda$ and $K^2 = \mathbf{K}\cdot\mathbf{K}$.

The function $B_0(\mathbf{P})$ is virtually representable (i.e., $b(\mathbf{K})$ approaches zero for K sufficiently greater than k, depending upon d) as the Fourier transform of a band-limited function, so a two-dimensional spatial sampling theorem can be used to determine $b(\mathbf{K})$. If $\pm k_{xm}$ and $\pm k_{ym}$ are the respective band limits on k_x and k_y, then $b(\mathbf{K})$ can be represented [1] as a double Fourier series with sample points

$$\mathbf{P}_{rs} = \frac{r\pi}{k_{xm}}\mathbf{a}_x + \frac{s\pi}{k_{ym}}\mathbf{a}_y$$

where $r, s = 0, \pm 1, \pm 2, \cdots$. In practice, $B_0(\mathbf{P}_{rs})$ is sampled over a finite aperture, which limits the number of sample points. Now if the FFT is used to evaluate (1), then the number of output data points will equal the number of input sample points. It will become apparent that a large output spectral density (number of data points) is required for near-field computations. Accordingly, we increase the output spectral density by zero filling around the scan area boundary. Setting $B_0(\mathbf{P}_{rs}) = 0$ for data points outside the scan area boundary and letting N_x and N_y designate the number of sample points along the x and y axes, we obtain

$$b(\mathbf{K}_{mn}) = \frac{1}{\lambda}\sqrt{\frac{2P_0}{\pi A_0 Y_0 G_r(0)}}\, e^{-i\gamma_{mn}d}\,\frac{\pi^2}{k_{xm}k_{ym}} \cdot \sum_{r=-(N_x/2)}^{(N_x/2)-1}\ \sum_{s=-(N_y/2)}^{(N_y/2)-1} B_0(\mathbf{P}_{rs})e^{-i\mathbf{K}_{mn}\cdot\mathbf{P}_{rs}} \quad (2)$$

where $-N_x/2 \leqq m \leqq N_x/2 - 1$, $-N_y/2 \leqq n \leqq N_y/2 - 1$. Here, $\mathbf{K}_{mn} = m\Delta_x\mathbf{a}_x + n\Delta_y\mathbf{a}_y$ and $\gamma_{mn} = \sqrt{k^2 - K_{mn}^2}$, where $\Delta_x = 2k_{xm}/N_x$, $\Delta_y = 2k_{ym}/N_y$. Normally, the sample point spacings $\delta_x = \pi/k_{xm} \cong \lambda/2$, $\delta_y = \pi/k_{ym} \cong \lambda/2$ apply.

We now return to the development of the near-field computation algorithm. The electric field is obtained from the plane-wave spectrum integration

$$\mathbf{E}(\mathbf{r}) = \frac{1}{2\pi}\iint_{-\infty}^{\infty}\mathbf{b}(\mathbf{K})e^{i\mathbf{k}\cdot\mathbf{r}}\,d\mathbf{K} \quad (3)$$

at any point $\mathbf{r} = \mathbf{R} + z\mathbf{a}_z$, where $\mathbf{R} = x\mathbf{a}_x + y\mathbf{a}_y$, $\mathbf{k} = \mathbf{K} + \gamma\mathbf{a}_z$ and $d\mathbf{K} = dk_xdk_y$. Here we assume that the vector spectral-density function $\mathbf{b}(\mathbf{K})$ is known. If both the x and y components of $\mathbf{b}(\mathbf{K})$ have been determined, then the z component is obtained from $b_z(\mathbf{K}) = -(1/\gamma)\mathbf{K}\cdot\mathbf{b}(\mathbf{K})$. In the far field of the antenna (3) becomes

$$\mathbf{E}(\mathbf{r}) \cong -ik\cos\theta\,\mathbf{b}\left(\frac{k}{r}\mathbf{R}\right)\frac{e^{ikr}}{r},$$

where $\cos\theta = z/r$ and $r = \sqrt{\mathbf{r}\cdot\mathbf{r}}$.

In the Fresnel region evanescent modes will not be significant, so the integration limits in (3) change from $\pm\infty$ to $\pm k$. The minimum applicable z distance is at least a few wavelengths to ensure attenuation of evanescent modes. Each integration is carried out by the FFT for one fixed value of z at a time. However, stability problems can become critical in carrying out a numerical integration. In particular, when z is moderately large, the factor $e^{i\gamma z}$ in the integrand can oscillate rapidly between ± 1 while the rest of the integrand changes very little. As a result, these terms cancel out analytically, but with discrete data on a computer they can add numerically to produce a significant integration error. This can occur when z/D is as small as 2 or 3, where D is the antenna diameter. One can compensate for this by limiting the domain of integration even further, say to $-k_{x0} \leqq k_x \leqq k_{x0}$, $-k_{y0} \leqq k_y \leqq k_{y0}$, where $k_{x0} < k$, $k_{y0} < k$. That is, we have to evaluate the near-field expression

$$\mathbf{E}(\mathbf{r}) = \frac{1}{2\pi}\int_{-k_{x0}}^{k_{x0}} e^{ik_x x}\,dk_x \int_{-k_{y0}}^{k_{y0}} e^{i\gamma z}\mathbf{b}(\mathbf{K})e^{ik_y y}\,dk_y. \quad (4)$$

We obtain integration-domain limits for (4) by using the sampling theorem criterion, namely, that the maximum change in γz between two adjacent sample points shall be less than π. This leads to the result

$$\frac{k_{x0} + k_{y0}}{k} \cong \frac{R_0}{\sqrt{R_0^2/\beta + z^2}} \quad (5)$$

where $R_0 \equiv \pi/\Delta_y \cong \pi/\Delta_x$ is the maximum lateral coordinate range. Here, $\beta = 1 + \sin 2\phi_0$, where $\phi_0 = \tan^{-1} k_{y0}/k_{x0}$. The dominant feature of this result is a bowed diamond-shaped integration domain. Equation (5) is derived in the Appendix, where we establish that the maximum z distance is limited to $z < R_0^2/\lambda$.

Using the FFT to evaluate (4), it is expedient to integrate over the extended domain $|k_x| \leqq k_{xm}$, $|k_y| \leqq k_{ym}$, where $k_{xm} \cong k_{ym} \geqq k$, and use a window function to limit the effective integration domain to $k_{x0} < k_{xm}$, $k_{y0} < k_{ym}$. Thus, for a fixed value of z, we can approximate (4) by

$$\mathbf{E}_{j,l} = \frac{\Delta_x\Delta_y}{2\pi}\sum_{m=-(N_x/2)}^{(N_x/2)-1}\ \sum_{n=-(N_y/2)}^{(N_y/2)-1}\mathbf{F}(m\Delta_x, n\Delta_y) \cdot \exp\left\{i2\pi\left(\frac{jm}{N_x} + \frac{ln}{N_y}\right)\right\}. \quad (6)$$

Here, $\mathbf{E}_{j,l}$ is the Fresnel-region electric field in the x–y plane corresponding to a fixed value of z with $x = j\delta_x$, $y = l\delta_y$. Also, $\mathbf{F}(k_x, k_y) = \mathbf{b}(\mathbf{K})u(\mathbf{K})e^{i\gamma z}$, where $u(\mathbf{K})$ is a window function for limiting the oscillatory behavior of $e^{i\gamma z}$. The extended integration domain limits are given by $k_{xm} = 1/2\,N_x\Delta_x$, $k_{ym} = 1/2N_y\Delta_y$. In (6), $-N_x/2 \leqq j < N_x/2$, $-N_y/2 \leqq l < N_y/2$, so the limits on R_0 are $|x| \leqq 1/2N_x\delta_x = \pi/\Delta_x$, $|y| \leqq 1/2N_y\delta_y = \pi/\Delta_y$. However, good numerical stability of (6) at moderately large z values limits the effective lateral coordinate range to about $|x| < 1/4N_x\delta_x$, $|y| < 1/4N_y\delta_y$. That is, the effective lateral range is $x_{\max} \cong y_{\max} = R_0/2$.

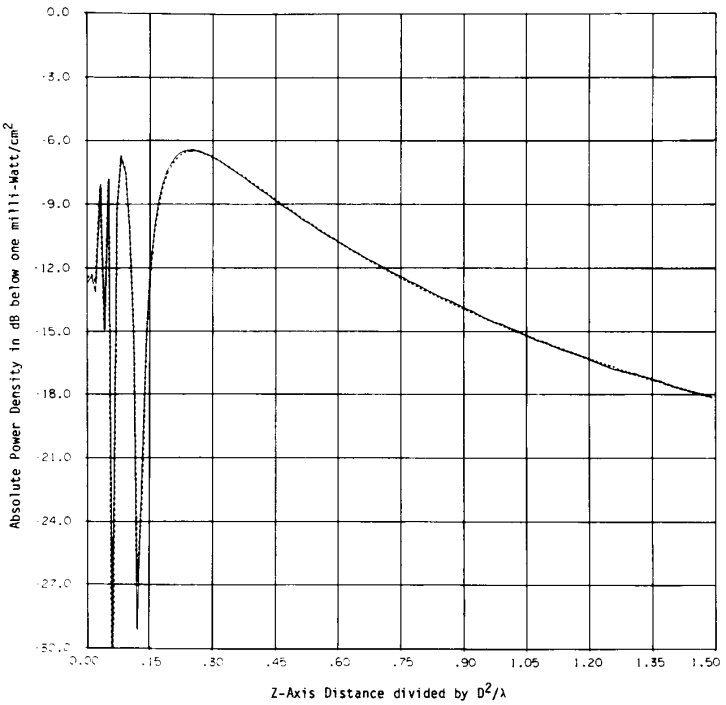

Fig. 2. Comparison of results, along z axis, as produced by planar program (solid line) and calculated using exact theoretical expression (dashed line) for 20-λ diameter uniformly excited circular aperture at 4 GHz showing power density in dB below one 1 mW/cm^2, assuming 1-W input power to aperture.

Note that this specification and the sample-point spacing increment together determine N_x and N_y.

The window function $u(\mathbf{K})$ is set to zero for $|k_x| + |k_y| > k_{x0} + k_{y0}$. However, checking for this condition requires the calculation of a square root and an arc tangent at each point. Accordingly, for ease of computation we ignore bowing of the diamond-shaped integration domain, applying instead a compensating domain expansion. In particular, replacing the right side of (5) with the criterion developed using the "sheaf of angles" analysis [2] yielded good results when the effective lateral range limit $1/2R_0$ was imposed. Thus $u(\mathbf{K})$ is set equal to zero when

$$\frac{|k_x| + |k_y|}{k} > \frac{R_0 + D}{\sqrt{R_0^2 + z^2}}.$$

The integration cutoff imposed by $u(\mathbf{K})$ can lead to ringing at the extremities of the computed near field when the amplitude of $\mathbf{b}(\mathbf{K})$ at the cutoff point is large. This, in fact, is the reason for limiting the effective range on x and y to about half the normal FFT output range. This range limitation quadruples the number of data points needed for the plane-wave-spectrum integration.

We now write (6) in a form more suitable for FFT processing. We assume $N_x/2$ and $N_y/2$ are even integers and that we can redefine j and l such that the ranges $0 \leqq j \leqq N_x - 1$, $0 \leqq l \leqq N_y - 1$ apply. For the case where we are interested in the field along the y axis when $x = 0$ we obtain

$$\mathbf{E}_{0,l-(N_y/2)} = \frac{\Delta_x \Delta_y}{2\pi} e^{-il\pi} \sum_{n=0}^{N_y-1} \cdot e^{in\pi} \left\{ \sum_{m=0}^{N_x-1} \mathbf{F}\left[\left(m - \frac{N_x}{2}\right)\Delta_x, \left(n - \frac{N_y}{2}\right)\Delta_y\right]\right\} e^{i2\pi nl/N_y}. \quad (7)$$

With this formulation, we simply sum along the k_x coordinate followed by a one-dimensional FFT on the k_y coordinate. A similar "one-dimensional collapse" formulation is used to compute the near field along the x axis.

III. Comparison of Computations versus Theoretical and Measured Data

Near-field computations using this algorithm were tested against both theoretical calculations and measured data. In Fig. 2 we compare results produced by the planar near-field program against an exact theoretical expression obtained by Rudduck and Chen [21] for the field along the z axis of a uniform circular aperture. The absolute power densities obtained by each method are compared for a 20 λ diameter circular aperture at an operating frequency of 4 GHz. Computed results are plotted as solid lines while theoretical

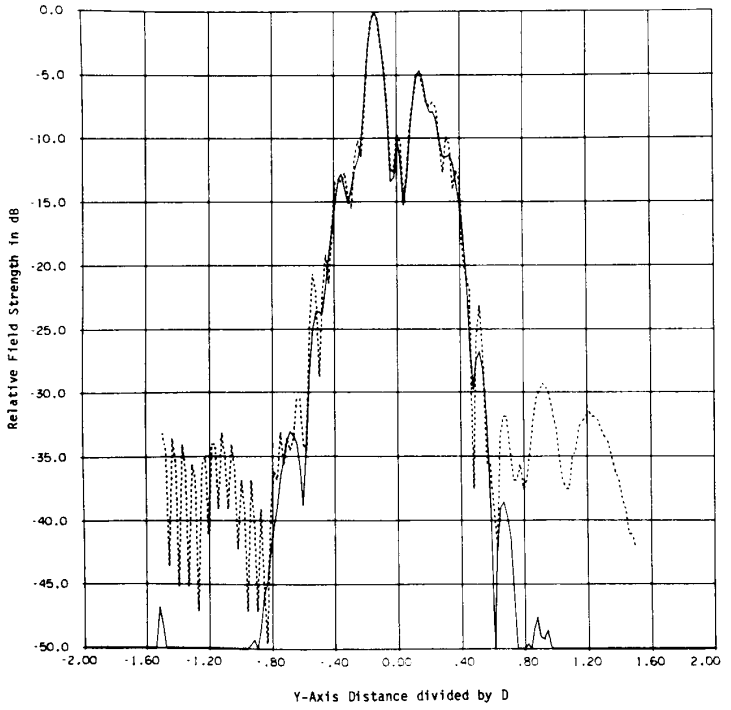

Fig. 3. Comparison of measured (dashed line) and computed (solid line) relative E-plane-cut field intensity curves for antenna 1 at z = 65.3 cm.

calculations are plotted as dashed lines. The on-axis electric field strength for a uniformly excited circular aperture is given by

$$E=\frac{1}{a}\sqrt{\frac{2P_0}{\pi Y_0}}\left[e^{ikz}-\frac{z}{R}e^{ikR}\right], \qquad R=\sqrt{z^2+a^2}$$

where $a = D/2$ is the aperture radius.

In Figs. 3–8 we compare computed results with measured data at corresponding z-axis distances. Dashed lines denote comparison measurements while solid lines denote computed results. Antenna 1 (Figs. 3–5) has a D/λ ratio of 16.2, while antenna 2 (Figs. 6–8) has a D/λ ratio of 77.6. For each antenna, measurements and computations for the field's dominant y component are compared at the measurement plane and at z-axis distances of 100 and 300 cm beyond that. The dB normalization of any graph is with respect to peak power in that antenna's measurement plane. Now the sides of the measurement plane's scan area are shorter than the length of the comparison scan. As a consequence, there are fewer recomputed near-field points than measured comparison points at the shortest distance.

The agreement shown between the near-field computations and both measured and theoretical results is remarkable in view of the very complex pattern structure of these near-zone fields. A typical set of computed near-zone y–z plane power-density contours is shown in Fig. 9 for antenna 1. These contours give absolute power density in dB(1 mW)/cm^2 corresponding to 1 W of input power at the antenna aperture.

With planar near-field measurements the computed far-field is valid throughout an angular region limited by an angle subtended by the distance from the edge of the scan plane to the projected edge of the test antenna [15]. Applying this determining criterion throughout the near-field, the results in Fig. 9 are valid up through an angle of about 35° measured from the edge of the aperture. However, due to foreshortening of the longitudinal axis the region of validity extends up through the farthest depicted contour. That is, all of the results presented in Fig. 9 are valid except for the small area at the extreme left where no contours are plotted. Also regarding Fig. 9, the FFT algorithm produced results for y-axis distances up to $\pm 4D$, but the presentation is limited to $\pm 2D$.

Computed near-zone power-density contours for antenna 2 are shown in Fig. 10. Here, results are valid up through an angle of about 45°, so once again all of the results shown are valid except at the extreme left in the figure where no contours are plotted.

IV. Prediction of Near Fields Radiated by Circular Apertures

Having a successful computation algorithm enables us to characterize near-field intensity levels for specific classes of antennas. There are many instances where such an estimate can be useful, such as electromagnetic compatability studies. The near fields are predicted by numerically integrating predetermined plane-wave spectrum data, obtained from analytical far-field expressions that are in turn generated by integrable aperture distribution functions. Here, we wish to

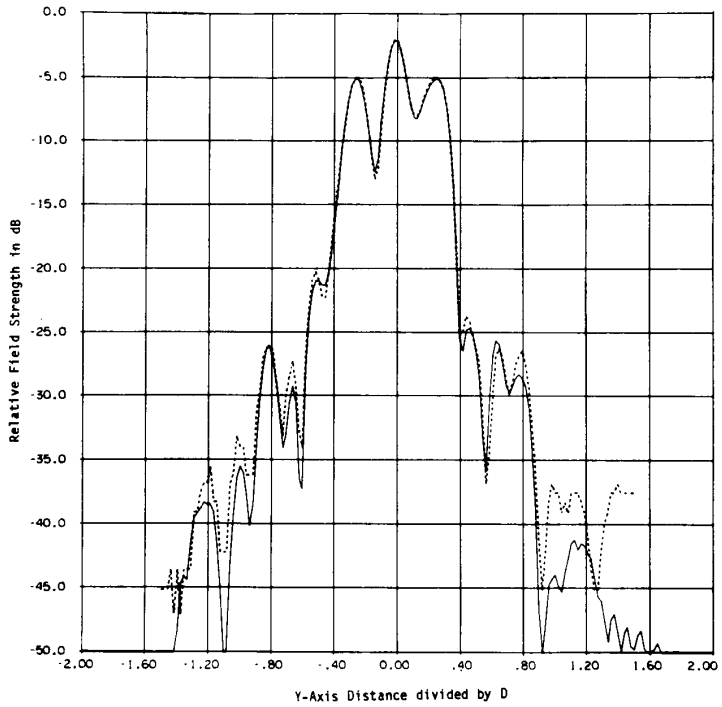

Fig. 4. Comparison of measured (dashed line) and computed (solid line) relative E-plane-cut field intensity curves for antenna 1 at z = 165.3 cm.

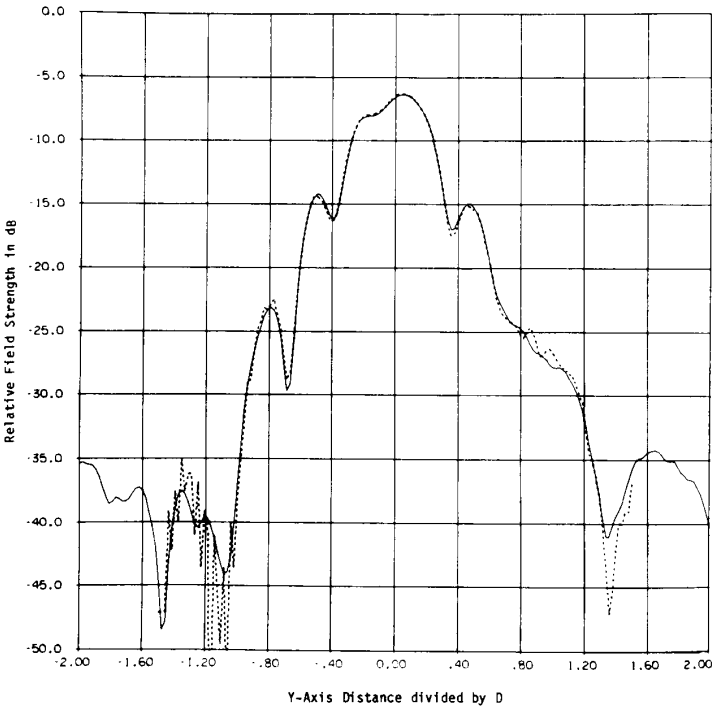

Fig. 5. Comparison of measured (dashed line) and computed (solid line) relative E-plane-cut field intensity curves for antenna 1 at z = 365.3 cm.

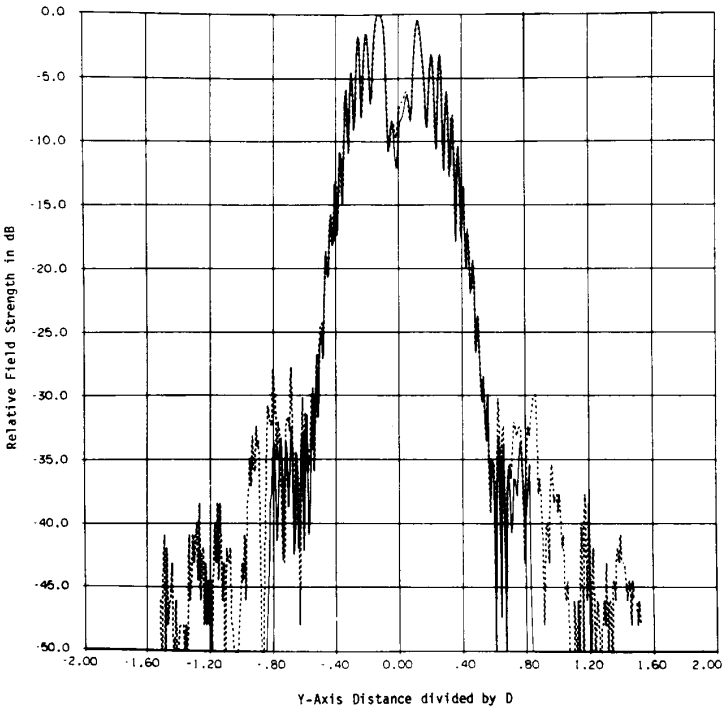

Fig. 6. Comparison of measured (dashed line) and computed (solid line) relative E-plane-cut field intensity curves for antenna 2 at z = 42 cm.

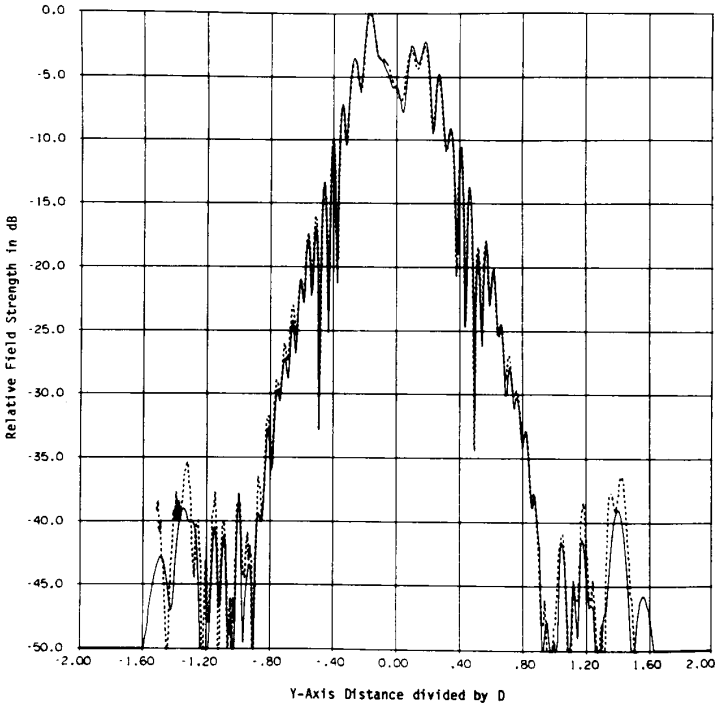

Fig. 7. Comparison of measured (dashed line) and computed (solid line) relative E-plane-cut field intensity curves for antenna 2 at z = 142 cm.

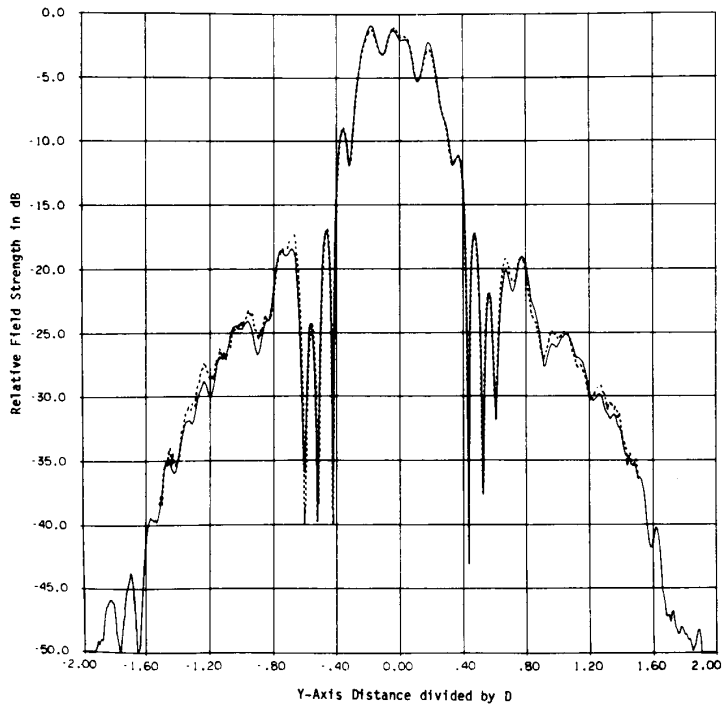

Fig. 8. Comparison of measured (dashed line) and computed (solid line) relative E-plane-cut field intensity curves for antenna 2 at z = 342 cm.

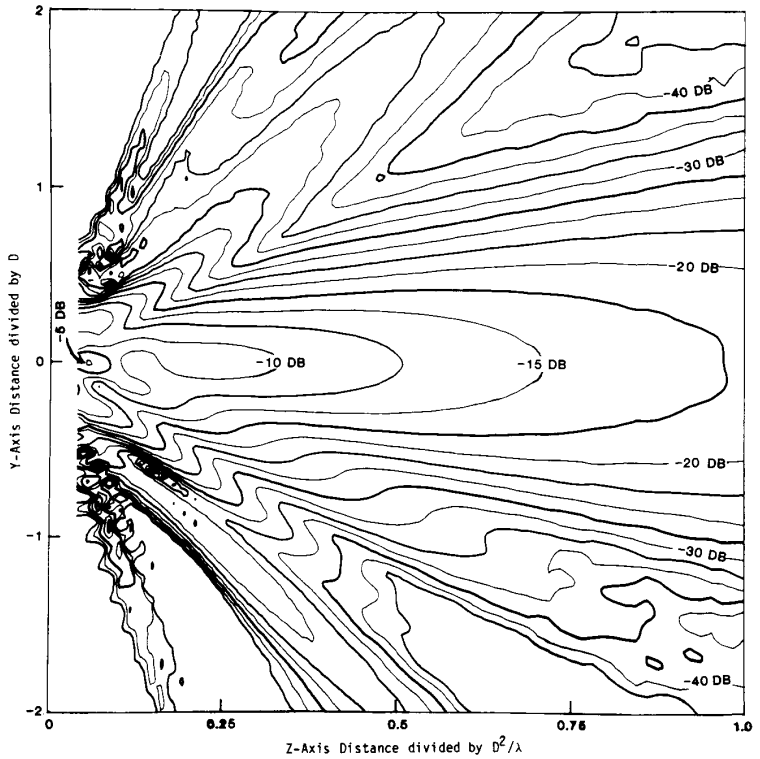

Fig. 9. Near-zone power density contour for antenna 1 in dB below 1 mW/cm^2 for 1-W input power to antenna (2.5 dB separation between adjacent contours).

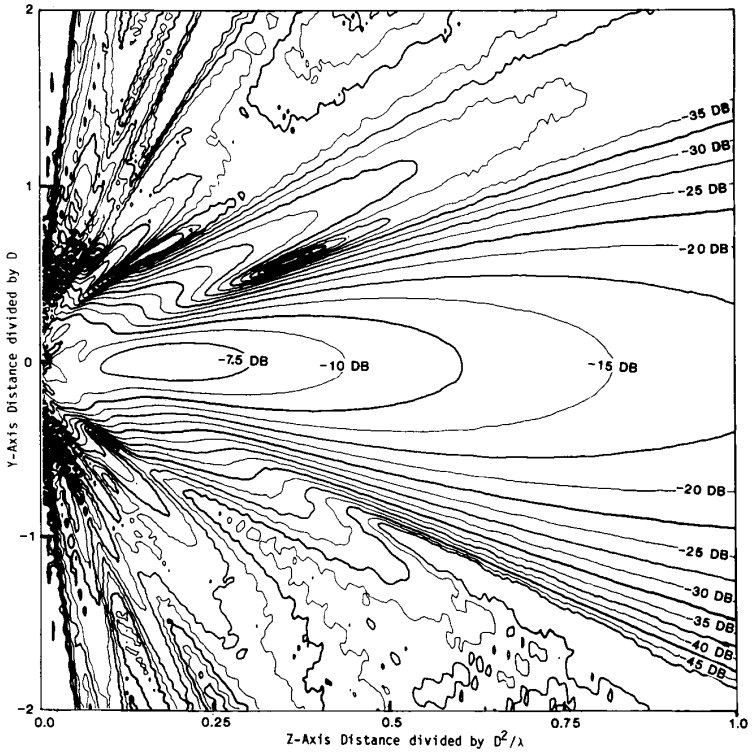

Fig. 10. Near-zone power density contour for antenna 2 in dB below 1 mW/cm^2 for 1-W input power to antenna (2.5 dB separation between adjacent contours).

model parabolic-dish antennas as a circular aperture with rotationally symmetric tapered illuminations.

The aperture distribution function chosen for study has the form $\alpha + [1 - (\rho/a)^2]^2$, where α is a small constant, ρ is the radial-distance variable in the aperture, $0 \leq \rho \leq a$, and $a = D/2$. We wish to plot relative power-density contours in the y–z plane, where the graph's abscissa extends from just in front of the antenna out to D^2/λ in units of D^2/λ and the ordinate covers the range 0 to $4D$ in units of D. As discussed earlier, with this choice of scaling and $D \geq 30\ \lambda$ one graph suffices to describe all antennas with the same relative aperture distribution function. For D/λ ratios less than 30, our graphical results apply only at proportionately smaller ordinates. A few such results are presented in [22].

In Fig. 11 we present power-density contours for the case $\alpha = 0$. The step between adjacent contours corresponds to 2.5 dB; also light and dark contours alternate. We obtain the absolute power density at any point in dB(1 mW)/cm^2 relative to 1 W of input power at the antenna aperture by adding the (negative) dB reading from this figure to the quantity, $38.57 - 20 \times \log D$, where D is in centimeters.

In Fig. 12 we present results corresponding to $\alpha = 0.1$ (a pedestal 20 dB down). Here, the absolute power density in dB/cm^2 for 1 W of input power is obtained by adding the relative dB reading from Fig. 12 to the quantity, $38.17 - 20 \times \log D$.

In applying the results of this section, note that aperture blockage, struts, and edge diffraction from the rim of the reflector may produce additional effects that have not been accounted for here. For instance, endfire (i.e., along the y axis) fields can be produced by edge diffraction resulting from feed spillover. However, except along the y axis a theoretical model of such effects (such as a torus function modeling the edge diffracted field radiated onto a hypothetical measurement plane) could be used to advantage with our technique.

To illustrate the use of these graphs, assume that the antenna is a 11.3-m (37-ft) diameter parabolic reflector operating at 6.5 GHz with 56 kW of input power and that we wish to estimate the power density 823 m (2700 ft) out from the antenna and 15.2 m (50 ft) off axis. Thus the transverse distance is 1.35 D and the longitudinal distance is 0.3 D^2/λ. From Fig. 11 the power density is about -45 dB relative to the peak field intensity, corresponding to -67.5 dB (1 mW)/cm^2 for each watt of input power or to an absolute power density of 0.01 mW/cm^2. According to Fig. 12, the effect of a pedestal at this location is destructive interference, so this estimate may be considered as worst case.

V. Conclusion

We have presented an improved algorithm for calculating near fields in the vicinity of radiating aperture or dish antennas, and we have demonstrated that our algorithm is capable of extremely high accuracy. We obtain numerical stability for our near-field integral expression by utilizing a diamond-shaped integration domain. Relative power-density contours are found to be a convenient and informative method for exhibiting results, and we have shown that a single set of

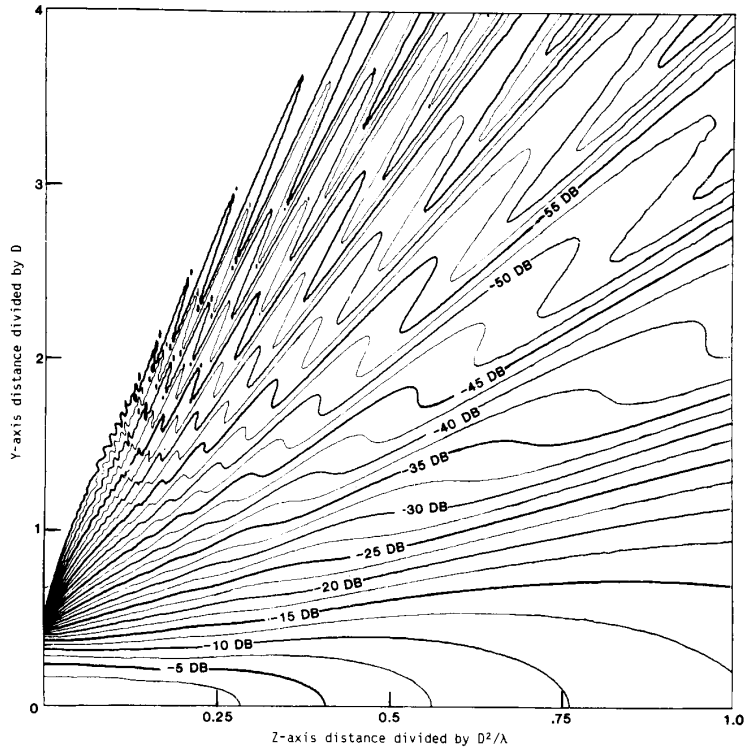

Fig. 11. Relative power density contour in y–z plane for $[1 - (\rho/a)^2]^2$ aperture distribution; $D > 30\ \lambda$.

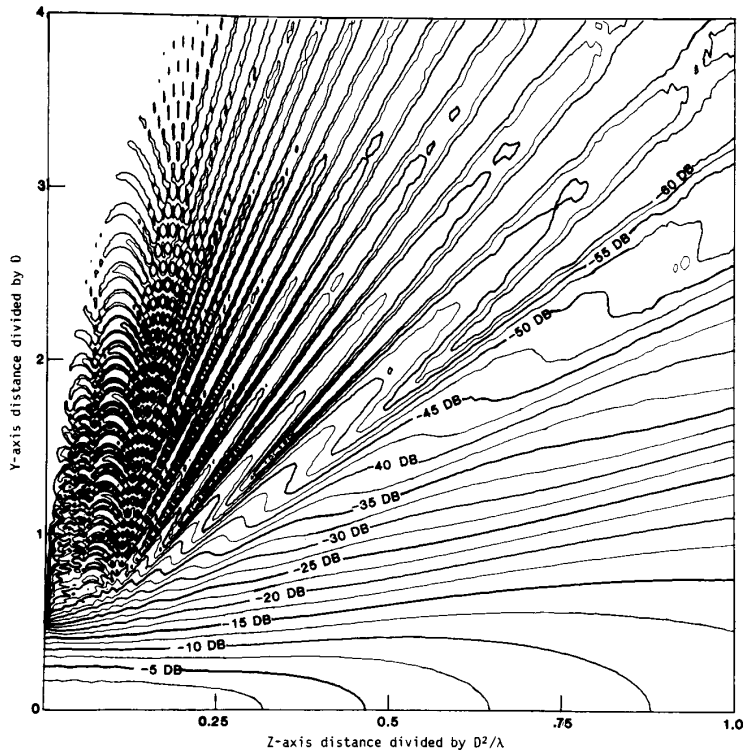

Fig. 12. Relative power density contours in y–z plane for $[1 - (\rho/a)^2]^2$ aperture distribution on pedestal 20-dB down; $D > 30\ \lambda$.

contours can be used to characterize near fields for a class of antennas that have similar aperture distribution functions. We presented typical power-density contours for two specific antennas along with nomographs and associated formulas for obtaining the absolute power density in the near field of a circular aperture of arbitrary size for two particular relative aperture distribution functions.

Appendix

Here, we wish to obtain integration limits k_{x0}, k_{y0} to bound the oscillatory behaviour of $e^{i\gamma z}$ in the integrand of (4). We do this by making use of the sampling theorem, which requires that there be at least two sample points per cycle at the greatest resolvable "z" spatial frequency. That is, k_{x0} and k_{y0} are determined so that the integrand will contain only those z-component spatial frequencies that satisfy this criterion; thus the maximum incremental change allowed in γ will be π/z. Since $\gamma = \sqrt{k^2 - K^2}$, where $K^2 = k_x^2 + k_y^2$, the applicable criterion for determining the integration domain limits is

$$\frac{\pi}{kz} = \sqrt{1-(U^2-b)} - \sqrt{1-U^2}. \tag{8}$$

Here $U \equiv K_0/k = \sqrt{k_{x0}^2 + k_{y0}^2}/k$ and b represents the small incremental change in U^2 corresponding to a change from the sample point k_{x0}, k_{y0} to the point $k_{x0} - \Delta_x$, $k_{y0} - \Delta_y$. For consistency we require that $k_{x0} + k_{y0} > \Delta_x + \Delta_y$.

The assumption that evanescent modes are negligible in (3) implies that $U < 1$. Accordingly, we can apply the binomial expansion, $\sqrt{1 - U^2} = 1 - (U^2/2) - (U^4/8) - \cdots$ to (8). After cancelling terms and rearranging series expansions, we obtain

$$\frac{\pi}{kz} = \frac{b}{8}\left(1 + \frac{1}{1-U^2} + \frac{2}{1-U^2/2} - \frac{U^8}{32} - \frac{5U^{10}}{64} - \cdots\right) - 0\left(\frac{b^2}{8}\right). \tag{9}$$

Neglecting terms of order b^2 or smaller, we can express b as the ratio of a fourth-order polynomial to a power series in U^2. Carrying out the indicated power-series division, we obtain

$$b = \frac{2\pi}{kz}\left(1 - \frac{U^2}{2} - \frac{U^4}{8} - \frac{U^6}{16} - \frac{5U^8}{128} - \frac{7U^{10}}{256} - \cdots\right). \tag{10}$$

Now let $\Delta \equiv \Delta_x \cong \Delta_y$. Then

$$k^2 b = K_0^2 - (k_{x0} - \Delta)^2 - (k_{y0} - \Delta)^2 = 2\Delta(k_{x0} + k_{y0} - \Delta)$$

or

$$kb = 2\Delta\left(\alpha U - \frac{\Delta}{k}\right)$$

where

$$\alpha = \cos\phi_0 + \sin\phi_0 \qquad \phi_0 = \tan^{-1}\frac{k_{y0}}{k_{x0}}.$$

We have $\Delta = \pi/R_0$ (see expressions following (2)), where $R_0 = \frac{1}{2}N_y\delta_y$ is the maximum lateral-coordinate range. Consequently, b^2 in (9) is negligible compared to b provided that $R_0 \gg \lambda$. Now we can express (10) as

$$U^2 + 2\frac{\alpha z}{R_0}U - \frac{\lambda z}{R_0^2} = 2 - \sigma \tag{11}$$

where $\sigma = (U^4/4) + (U^6/8) + (5U^8/64) + \cdots$. We solve (11) as a simple quadratic equation in U. Then, for $z > R_0$ and neglecting terms smaller than $(\lambda/R_0)^2$, we expand the resulting radical as a power series in $R_0/\alpha z$ including the small correction term σ in the expansion. Iteratively substituting successive terms of the $R_0/\alpha z$ power series into the expression for σ we obtain a corrected series expansion for U, which to an accuracy of $(R_0/\alpha z)^{13}$ is equivalent to the power series expansion of

$$U = \frac{1}{\sqrt{\left(\frac{\alpha z}{R_0}\right)^2 + 1 + \frac{\lambda z}{R_0^2}}} + \frac{\lambda}{2\alpha R_0}. \tag{12}$$

Equation (12)'s greatest source of discrepancy comes from neglecting the b^2 terms in (9), so for z large the discrepancy in U is on the order of $\lambda R_0/4\alpha z^2$. Thus, for $z/R_0 > (R_0/\lambda)^{1/2}$, the discrepancy is less than $(\lambda/R_0)^2$. From (12) we readily see that our consistency condition $k_{x0} + k_{y0} > 2\Delta$ is satisfied provided $z < 2R_0^2/\lambda$. Finally, neglecting terms of order λ/R_0, (12) becomes

$$U = \frac{1}{\sqrt{\left(\frac{\alpha z}{R_0}\right)^2 + 1}}.$$

References

[1] D. M. Kerns, *Plane-Wave Scattering-Matrix Theory of Antennas and Antenna-Antenna Interactions*. Nat. Bur. Stand. Monograph 162, June 1981.

[2] A. D. Yaghjian, "Efficient computation of antenna coupling and fields within the near-field region," *IEEE Trans. Antennas Propagat.*, vol. AP-30, pp. 113-128, Jan. 1982.

[3] R. C. Hansen, *Microwave Scanning Antennas, vol. 1—Apertures*. New York: Academic, 1964.

[4] A. W. Rudge, K. Milne, A. D. Olver, and P. Knight, *The Handbook of Antenna Design*, vol. 1. London: Peter Peregrinus, 1982.

[5] J. Brown, "Theoretical analysis of some errors in aerial measurements," *Proc. Inst. Elec. Eng.*, vol. 105C, pp. 343-351, Feb. 1958.

[6] J. Brown and E. V. Jull, "The prediction of aerial radiation patterns from near-field measurements," *Proc. Inst. Elec. Eng.*, vol. 108B, pp. 635-644, Nov. 1961.

[7] D. M. Kerns, "Correction of near-field antenna measurements made with an arbitrary but known measuring antenna," *Electron. Lett.*, vol. 6, pp. 346-347, May 1970.

[8] A. C. Newell and D. M. Kerns, "Determination of both polarization and power gain of antennas by a generalized 3-antenna measurement method," *Electron. Lett.*, vol. 7, pp. 68-70, Feb. 1971.

[9] F. Jensen, "Electromagnetic near-field far-field correlations," Ph.D. dissertation, Tech. Univ. Denmark, Lyngby, 1970.

[10] A. C. Ludwig, "Near-field far-field transformations using spherical-wave expansions," *IEEE Trans. Antennas Propagat.*, vol. AP-19, pp. 214-220, 1971.

[11] R. C. Johnson, H. A. Ecker, and J. S. Hollis, "Determination of far-field antenna patterns from near-field measurements," *Proc. IEEE*, vol. 61, pp. 1668-1694, Dec. 1973.

[12] W. M. Leach, Jr., and D. T. Paris, "Probe compensated near-field measurements on a cylinder," *IEEE Trans. Antennas Propagat.*, vol. AP-21, pp. 435–445, July 1973.
[13] W. H. Kummer and E. S. Gillespie, "Antenna measurements—1978," *Proc. IEEE,* vol. 66, pp. 483–507, Apr. 1978.
[14] A. C. Newell, R. C. Baird, and P. F. Wacker, "Accurate measurement of antenna gain and polarization at reduced distances by an extrapolation technique," *IEEE Trans. Antennas Propagat.*, vol. AP-21, pp. 418–431, July 1973.
[15] A. C. Newell and M. L. Crawford, "Planar near-field measurements on high performance array antennas," Nat. Bur. Stand. Rep. NBSIR-74-380, July 1974.
[16] A. C. Newell, "Planar near-field measurement techniques," Nat. Bur. Stand., short course on antenna parameter measurement by near-field techniques lecture notes, July 1975.
[17] A. D. Yaghjian, "Upper-bound errors in far-field antenna parameters determined from planar near-field measurements, Part 1: Analysis," Nat. Bur. Stand. Tech. Note 667, Oct. 1975.
[18] A. C. Newell, "Upper-bound errors in far-field antenna parameters determined from planar near-field measurements, Part 2: Analysis and computer simulation," Nat. Bur. Stand., short course on antenna parameter measurement by near-field techniques lecture notes, July 1975.
[19] D. M. Kerns, "Plane-wave scattering-matrix theory of antenna and antenna-antenna interactions: formulation and applications," *J. Res. NBS-B,* vol. 80B, pp. 5–51, Jan.–Mar. 1976.
[20] H. J. Landu, "Sampling, data transmission, and the Nyquist rate," *Proc. IEEE,* vol. 55, pp. 1701–1706, Oct. 1967.
[21] R. C. Rudduck and C. L. J. Chen, "New plane-wave spectrum formulations for the near field of circular and strip apertures," *IEEE Trans. Antennas Propagat.*, vol. AP-24, pp. 438–449, July 1976.
[22] R. L. Lewis and A. C. Newell, "An efficient and accurate method for calculating and representing power density in the near-zone of microwave antennas," U.S. Dept of Commerce Nat. Bur. Stand. NBSIR 85-3036, Dec. 1985.

Richard L. Lewis (S'58–M'74–SM'82), for a photograph and biography please see page 1380 of the December 1987 issue of this TRANSACTIONS.

Allen C. Newell (M'73–M'81–SM'83), for a photograph and biography please see page 733 of this issue.